### Nuclear Spin Control in GaAs Quantum Dots via Nuclear Quadrupole Resonance

Leonardo S. Cardinale

Visiting student supervised by Dorian A. Gangloff, Department of Engineering Science, University of Oxford

leonardo.cardinale@ens.psl.eu

February 2023

Quantum dots (QDs) are an attractive system for quantum information storage and processing in a network. In a QD, an optically active electron is coupled to neighboring nuclei via the hyperfine interaction, which can be used to transfer electron spin states to this nuclear register with significantly longer coherence times, effectively realizing quantum memory. Protocols implementing such a memory are based on accurate and efficient control of the nuclear spin register. Incidentally, nuclear spin control methods are also vital to improving electron spin coherence, which is limited by the nuclear Overhauser field — the effective field arising from the interaction between the central spin and the mean spin polarization of neighboring nuclei. Nuclear spins are traditionally controlled via nuclear magnetic resonance (NMR), a technique based on the coupling of a particle's spin to a radio-frequency magnetic field tuned to the frequency of a transition between Zeeman-split energy levels. While this method has been fruitful, it is constrained by the requirement of driving large currents in proximal coils. Our goal is to develop a new way of inducing nuclear spin transitions in GaAs QDs using nuclear quadrupole resonance (NQR), a method based on the quadrupolar coupling between the spin-3/2 nuclei and an oscillating electric field gradient (EFG). Two avenues can be pursued to this end: one uses strain waves, the other uses AC quadrupole antennae etched onto the GaAs device hosting the QDs. One advantage of the latter is that QDs are addressed locally; the present work focuses on this approach. We propose an ideal model and simulation results of Rabi frequencies of nuclear spin rotation for given antenna geometries and QD depth. Furthermore, we show that electron energy levels can be protected from dipole fields, which might cause undesired DC Stark shifts on QD charge states and exciton energy. Further work will cover resonant circuit driving of the quadrupole antennae to reach EFGs sufficient for kHz to MHz Rabi frequencies on the nuclei. Our findings serve as a proof of concept for a promising alternative to NMR which could be implemented experimentally in the future.

### **Preface**

The work presented here is the result of a semester-long internship in the Quantum Engineering group at the University of Oxford, under the supervision of Prof. Dorian Gangloff. The group focuses on both theoretical and experimental aspects of solid-state spin and photon physics, contributing to the long-term

goal developing quantum computing and communication technologies. During my internship, I worked on the theoretical aspects of nuclear spin control in semiconductor quantum dots, resorting to both pen-and-paper modeling and computer simulation to derive the results below.

I'm very grateful to Prof. Dorian Gangloff for having me in his group and granting me so much of his invaluable time. This internship has confirmed my desire to pursue research in physics, and has also shown me how quantum mechanics comes alive in real implementable systems. I'd also like to thank Ahmed Hassanen, Khadija Sarguroh, Dr. Andreas Thurn and Dr. Christian Schimpf for their support and friendship, as well as for fascinating physics discussions. A special thanks is also in order to Martin Wafula for being incredibly welcoming and making me feel at home at the Department of Engineering Science.

### Contents

1	Introduction	3
	1.1 Background	3
	1.2 Semiconductor quantum dots	3
	1.3 The hyperfine interaction and quantum memory	4
2	Nuclear quadrupole resonance	5
	2.1 The nuclear quadrupole Hamiltonian	5
	2.2 Resonant driving of nuclear spin transitions	6
	2.3 Detecting Rabi oscillations	6
3	Models and simulations of EFGs and Rabi frequencies	7
	3.1 Rabi frequencies as a function of EFG principal component	7
	3.2 A toy model	8
	3.3 A realistic model	8
	3.3.1 Cubic electrodes	8
	3.3.2 Elongated electrodes with pointed extremities	9
4	Experimental considerations	12
	4.1 Resonant circuit driving of the antenna	12
	4.2 Canceling dipole fields	15
5	Conclusion	16
6	Appendix: Derivation of the quadrupole Hamiltonian	16

### 1 Introduction

### 1.1 Background

The advent of quantum computing will yield polynomial or even exponential speedups relative to classical algorithms, such as in the case of Grover's and Shor's algorithms respectively [1–4], and will also significantly improve simulations of inherently quantum mechanical systems [5]. Quantum computing relies on engineering the best possible quantum bit, or qubit, which is realized using a two-level quantum system which can be driven using quantum gates [2]. There are numerous two-level systems which can be used as qubits. For example, one can consider the energy levels of any spin-1/2 system – such as an electron – whose energy levels are split by the presence of a magnetic field, the energy levels of an atom treated in the two-level approximation, or photon polarization. As for quantum gates, in the first case one can consider the action of magnetic radio-frequency pulses transverse to a constant magnetic field [6, 7], in the second case the action of a laser, and in the third various optical components and even measurement [8].

Currently, the main candidates for qubits include superconducting qubits [9], photons [10], trapped ions [11], cold atoms, NV centers in diamond, and semiconductor quantum dots [12, 13], to which can be added hybrid platforms such as those based on rare-earth elements [14]. The present work focuses on nuclear spin control in quantum dots. Quantum dots (QDs) are particularly attractive, in that they involve an electron spin, the epitome of a qubit, which serves as an ideal source of single and entangled photons [15-17], and can transfer its state to neighboring nuclei, thereby achieving quantum memory [18]. Moreover, QDs are scalable systems and can be organized in a network, where each node can store information [19], making them an attractive solid-state platform for quantum computing.

### 1.2 Semiconductor quantum dots

There are various ways in which QDs can be formed. Interface fluctuation QDs can be created spontaneously when superimposing semiconductor materials of different bandgaps. Suppose we sandwich a thin layer of width d of GaAs between barriers of Al-GaAs. This configuration can be approximated by an infinite square well, which yields a ground state energy proportional to  $d^{-2}$ . However, there are also lateral fluctuations at the interface between the GaAs layer and the AlGaAs, which cause variations of d in the x-y plane (assuming the planes are superimposed along the z-axis). Thus, an electron will preferentially be present in the area of lowest energy and will be confined in all three dimensions [20].

Another way to form QDs is self-assembly by lattice-mismatched growth, such as in the case of InAs QDs. In this process, the semiconductor material in question is grown on a substrate that has a slightly different lattice constant, resulting in a mismatch of crystal lattices. This induces strain in the former, which consequently minimizes its surface energy by forming QDs [21].

GaAs, the semiconductor material used in this study, is formed using droplet etching. Small droplets of metal, such as gallium, are deposited on a GaAs material, which is subsequently annealed at a high temperature, thus causing the diffusion of metal atoms into the substrate. The GaAs/metal alloy acts as a template for QDs, which form upon exposing the substrate to a source of GaAs [22].

The confinement along the growth direction (z-axis for our purposes) of the semiconductor is stronger than that in the x-y plane. Thus, we can approximate the confinement potential for an electron in a QD by a radially symmetric 2D harmonic potential [20]. This confinement results in atom-like energy levels in the QD. However, the semiconductor band structure remains, and as such emission and absorption are accompanied by exciton creation and photoluminescence [20]. Therefore, the ground state is characterized by the presence of one electron, while in the first excited state the electron is joined by an exciton, or electron-hole pair; the QD can transition between different states via photon emission or absorption [23]. In atomic physics, additional effects which modify the energy levels of the electron can be taken into account via perturbation theory. These include the fine structure, spin-orbit coupling and the

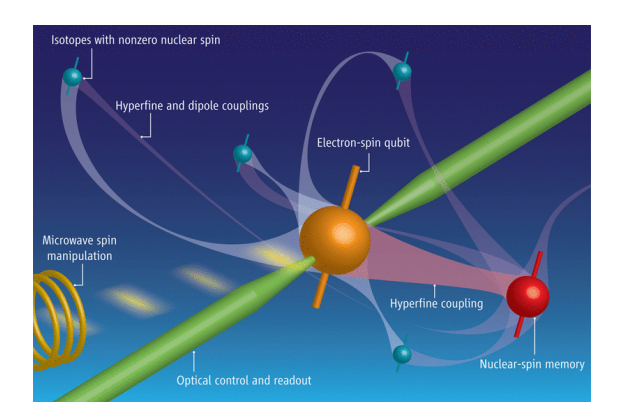


Figure 1: Illustration of the interactions in a QD. A central electron-spin qubit (in orange) is coupled via the hyperfine and dipole interactions with neighboring nuclei (in blue), some of which are used for quantum memory (in red). The green beam passing through the central spin represents optical control and readout of the spin state, while the yellow coil represents spin manipulation via NMR [24].

hyperfine structure. These additional factors are also present in QD physics, and the latter enables one to use QD nuclei as a quantum memory.

## 1.3 The hyperfine interaction and quantum memory

In QDs, qubits are realized using a central optically active electron spin, whose energy levels are Zeemansplit using a static magnetic field, confined in all directions to length scales of the order of 10 nm and surrounded by  $10^4 - 10^6$  nuclei [25]. The electron can thus be driven with electromagnetic radiation, and its state can be read out using spin selective optical transitions. Electrons in QDs can have coherence times of the order of 0.1 ms [26], whereas nuclei can achieve coherence times of the order of 10 ms [27]. Coherence times limit the duration of the total number of quantum gates in a given algorithm admissible in experiments, and as such they need to be maximized in order to satisfy DiVincenzo's criteria [28]. Using the hyperfine interaction between the

central electron spin and neighboring nuclear spins, one can induce a spin state transfer from the central electron to the nuclear spin register. Since nuclei display significantly longer coherence times, this scheme can be used to achieve quantum memory [18]. To operate a quantum memory, one needs to make sure the states transferred to nuclei are preserved. This can be done by applying dynamical decoupling to the nuclei, which requires a long series of pulses and as such efficient spin control. Another manifestation of the hyperfine interaction is the nuclear Overhauser field. Indeed, the central electron spin interacts with at least 10<sup>5</sup> nuclear spins, which can be accounted for in a mean-field approach as the interaction of the electron spin with an effective magnetic (Overhauser) field [23] generated by the mean nuclear polarization. This interaction shifts electron energy levels, limits electron coherence, and must be suppressed under usual circumstances [27, 29].

Much like in the case of atoms, the hyperfine interaction has three contributions: the interaction of the nuclear magnetic dipole moment with the magnetic field produced by the relative motion of the electron, a dipole-dipole interaction, and a contact interaction due to the fact that the nucleus has a spatial extension and thus "overlaps" with the wavefunction of an electron. Moreover, the latter effect is predominant in the case of an s-shell electron [30], which is a common case. The Fermi-contact hyperfine interaction between an electron and N nuclei in the QD is given by [23, 30]:

$$\hat{H}_{hf} = \frac{\nu_0}{2} \sum_{j} A^j |\psi(\vec{r}_j)|^2 \left( 2\hat{I}_z^j \hat{S}_z + \left[ \hat{I}_+^j \hat{S}_- + \hat{I}_-^j \hat{S}_+ \right] \right)$$

$$= \hat{H}_{OH} + \sum_{j} a_j \left( \hat{I}_+^j \hat{S}_- + \hat{I}_-^j \hat{S}_+ \right)$$
(1.1)

where  $\nu_0$  is the two atom cell volume,  $\vec{r}_j$  is the position vector of the j-th nucleus, and we use the ladder operators for electron spin  $\hat{S}_{\pm}$  and nuclear spin  $\hat{I}_{\pm}$ . To explain electron spin transfer to nuclear spin states, we focus on the spin-flip term, or collinear term, and denote the Overhauser Hamiltonian by  $\hat{H}_{OH}$ .

For N nuclei surrounding a central electron, the

quantum state is a product state. If we start with a fully polarized nuclear bath and a spin-down electron, the initial state is given by  $|\downarrow\rangle\otimes|0\rangle$  where  $|0\rangle=|I_0,...,I_0\rangle$ . By driving the electron spin on resonance with an effective magnetic field accounting for Overhauser splitting i.e. working in the eigenbasis of a Hamiltonian including both Zeeman and Overhauser fields, we can induce Rabi flopping between states  $|\downarrow\rangle\otimes|0\rangle$  and  $|\uparrow\rangle\otimes|1\rangle$ , where  $|1\rangle=\left(\sum_j|a_j|^2\right)^{-1/2}\sum_ja_j\,|I_0,...,(I_0-1)_j,...,I_0\rangle$ , thus producing a delocalized single-spin excitation, or spin wave (magnon) [18, 31]. For a Rabi angular frequency  $\Omega$ , letting this process go on for  $t=\frac{\pi}{\Omega}$  leads to the following transition:

$$(\alpha \mid \uparrow \rangle + \beta \mid \downarrow \rangle) \otimes \mid 0 \rangle \rightarrow \mid \uparrow \rangle \otimes (\alpha \mid 0 \rangle + i\beta \mid 1 \rangle) \quad (1.2)$$

Thus, once can effectively map the spin state of the electron onto the polarization states of the nuclei. As in the case of the nuclear Overhauser splitting, nucleus-nucleus dipole interactions act as noise limiting magnon coherence, which further justifies the development of nuclear spin control methods.

However, in GaAs QDs, the gallium and arsenic nuclei are spin-3/2 systems. In order to define and address a single two-level collective nuclear system as previously described by the  $|0\rangle$  and  $|1\rangle$  states, the four energy levels of a given nucleus need to be split into two-level sub-systems. This can be done by introducing anharmonicity to the energy levels of a nucleus using static strain [32].

# 2 Nuclear quadrupole resonance

## 2.1 The nuclear quadrupole Hamiltonian

The goal of this work is to control nuclear spins in semiconductor quantum dots using nuclear quadrupole resonance (NQR). Traditional methods of controlling spins are based on nuclear magnetic resonance (NMR), where one drives spin transitions using a magnetic radio-frequency pulse to perturb a

Zeeman-split system. The perturbation arises from the fact that the additional time-dependent magnetic field couples to the magnetic dipole moment of a particle which has non-zero spin, which is in turn proportional to the appropriate spin operator via the gyromagnetic ratio.

In the case of NQR, the perturbation is associated with the coupling of a nuclear quadrupole moment to an electric field gradient (EFG). Indeed, the nuclei we will consider have spin 3/2, and generally systems of spin I>1/2 have a quadrupole moment according to the Wigner-Eckart theorem [7] (see appendix for derivation) .

The QDs considered here for NQR are GaAs QDs. The advantage of using lattice-matched GaAs instead of InGaAs, another platform often used in QD experiments, is the lack of significant static inhomogeneous strain, which tends to produce unwanted electric field gradients (EFG) that have to be accounted for in NQR. Additional EFGs would also limit electron coherence [26].

Here, we will look into generating oscillating EFGs using multipole antennae. Another possible avenue for generating time-dependent EFGs uses strain waves, although this is not discussed here. Multipole antennae are particularly interesting in that they allow control of a specific set of QDs, rather than of the entirety of a sample.

The models and simulations in this work show that the quadrupole configuration is optimal for a given antenna. Indeed, the dipole configuration yields lower EFGs, while adding electrodes has a negligible effect on the orders of magnitude predicted. Hence, we shall exclusively be focusing on quadrupole antennae.

The Hamiltonian considered in NQR is given by a time-independent contribution, the potential energy of the nuclear magnetic dipole in the external Zeeman field, and a time-dependent one, the potential energy of the nuclear electric quadrupole in a time-dependent EFG [7, 30, 33]:

$$\hat{H} = \hat{H}_0 + \hat{H}_Q = \hbar \omega_L \hat{I}_z + \frac{eQ}{2I(2I-1)} \hat{I} \cdot \hat{V}(t) \cdot \hat{I}$$
 (2.1)

where  $\omega_L = -\gamma B$  is the Larmor frequency of the

studied nucleus of gyromagnetic ratio  $\gamma$ , and we assume that the static magnetic field is of the form  $\vec{B} = B\vec{e_z}$ . Q is the quadrupole moment and V is the EFG at the position of the nucleus.

#### 2.2Resonant driving of nuclear spin transitions

We will be driving transitions using a sinusoidal EFG oscillating close to the frequency of a given spin transition. We therefore consider an EFG of the form  $V\cos\omega t$ .

$$\hat{H}_Q(t) = \frac{eQ}{2I(2I-1)} \left( \hat{I} \cdot \hat{V} \cdot \hat{I} \right) \cos \omega t \qquad (2.2)$$

According to time-dependent perturbation theory, considering the following ansatz:

$$|\psi(t)\rangle = \sum_{k} c_k(t)e^{-\frac{iE_k t}{\hbar}} |k\rangle$$
 (2.3)

where  $E_k$  is the eigenvalue of  $\hat{H}_0$  associated with the eigenstate  $|k\rangle$ , yields the following differential equations for suitable n:

$$\dot{c}_n = -\frac{ieQ}{2I(2I-1)\hbar} \sum_k e^{\frac{i(E_n - E_k)t}{\hbar}} \langle n | \hat{I} \cdot \hat{V} \cdot \hat{I} | k \rangle \cos(\omega t) c_k$$
 For transitions of one unit of spin, this yields:

We thus obtain a system of n coupled linear differential equations with time-dependent coefficients. An additional approximation is used to derive analytical solutions, since we are not necessarily interested in using any angular frequency  $\omega$ , but rather resonance frequencies for different transitions. Using the rotating wave approximation, and applying the aforementioned result to spin-3/2 nuclei such as gallium and arsenic, we conclude that driving a transition from the  $|i\rangle$  state to the  $|i\rangle$  state implies the following Rabi frequency:

$$\Omega_{ij} = \frac{eQ}{6\hbar} \left| \langle i | \hat{I} \cdot \hat{Y} \cdot \hat{I} | j \rangle \right| \tag{2.5}$$

### **Detecting Rabi oscillations**

There are already well-established techniques used to measure Rabi oscillations in a macroscopic nuclear spin system. In NMR, this can be achieved by deriving the net magnetization of a sample using the density matrix formalism, and converting the oscillating magnetization into a measurable electrical signal [7]. The same ideas can be used for NQR. At thermal equilibrium at a temperature T, using the usual constant convention  $\beta = 1/k_BT$ , the density matrix is given by:

$$\rho_0 = \frac{1}{4}I + \beta\hbar\omega_L \begin{pmatrix} -\frac{3}{8} & 0 & 0 & 0\\ 0 & -\frac{1}{8} & 0 & 0\\ 0 & 0 & \frac{1}{8} & 0\\ 0 & 0 & 0 & \frac{3}{8} \end{pmatrix}$$
(2.6)

According to previous analysis, the harmonic perturbation given by the quadrupole interaction "rotates" nuclear spin states at an angular frequency  $\Omega/2$ . Hence, the density matrix at time t is given by  $\rho_t = R \rho_0 R^{\dagger}$  where R is the rotation matrix associated with the nuclear spin transition. We can then derive the i-the component of the net magnetization using:

$$M_i = \gamma \langle \hat{I}_i \rangle = \gamma \operatorname{Tr} \left( \rho_t \hat{I}_i \right)$$
 (2.7)

(2.8)

transitions of one unit of spin, this yields: 
$$M_z = \frac{N\gamma^2\hbar^2B}{k_BT} \left(\frac{1}{4}\cos\left(\Omega_1 t\right) + 1\right) \tag{2.8}$$

For transitions of two units of spin:

$$M_z = \frac{N\gamma^2\hbar^2 B}{k_B T} \left(\cos\left(\Omega_2 t\right) + \frac{1}{4}\right) \tag{2.9}$$

NOR induces oscillation along the static magnetic field axis, the z-axis, which doesn't necessarily coincide with the growth direction of the semiconductor. At 4 K, the typical temperature at which QD experiments are conducted, this magnetization is negligible. Rather, nuclei are magnetized by repeatedly transferring energy from the electron, via dynamic nuclear polarization. This leads to an effective temperature for the nuclei much lower than 4 K, allowing the above quantities to be measured.

In the specific case of QDs, one can also use the Overhauser splitting of the electronic energy levels to detect Rabi oscillation. Indeed, again using a mean-field approach to the hyperfine interaction and a simplified, uniform electron wavefunction, one obtains the following hyperfine interaction Hamiltonian [23]:

$$\hat{H}_{hf} = \frac{2\tilde{A}}{N} \langle \hat{I}_z \rangle \hat{S}_z = \frac{2\tilde{A}}{\gamma N} M_z \hat{S}_z$$
 (2.10)

We can then use the expressions of  $M_z$  derived above and inject it into the following electron transition energy, taking  $\omega_{Le}$  to be the Larmor frequency of the electron in the constant magnetic field:

$$\Delta E = \hbar \left( \omega_{Le} + \frac{2\tilde{A}}{\gamma N} M_z \right) \tag{2.11}$$

Thus, we can use spectroscopy to verify that the nuclei are indeed undergoing Rabi flopping [27]. In practice we'd also need to include longitudinal (spin-lattice, characteristic time  $T_1$ ) and transverse relaxation (spin-spin, characteristic time  $T_2$ ) [30]. These parameters must be taken into consideration in experiments; for example, the measured signal is reduced by a factor of  $\Omega T_1$  after each oscillation.

### 3 Models and simulations of EFGs and Rabi frequencies

## 3.1 Rabi frequencies as a function of EFG principal component

In this section, we develop a model which predicts EFGs, and by extension Rabi frequencies for different geometries of the apparatus described in the following lines. Since the wavelengths associated with resonance frequencies are significantly larger than the dimensions of the quantum dot and electrodes we will be studying, we opt for a quasistatic approach rather than a radiation-based study. We will be using electrodes forming a quadrupole with sinusoidally oscillating electric potentials. The quasistatic approach

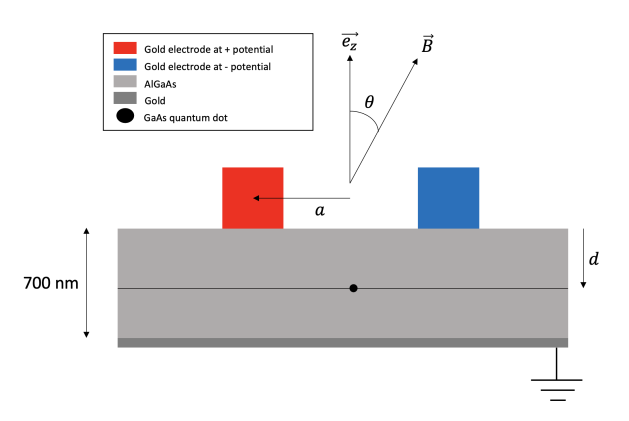


Figure 2: Side view of the system: an AlGaAs substrate with GaAs QDs located on a line of varying depth d, and four electrodes, each placed at a distance a from the origin.

allows us to consider at a given time t a Dirichlet problem with boundary conditions on the electrodes and a ground plane, which we solve for a potential distribution, which in turn gives us an EFG. If the sinusoidal electrode potential is  $V_0 \cos \omega t$ , we can use  $V_0$  in the boundary conditions for the Dirichlet problem. Once we've solved for the EFG Y (which one can check is proportional to the electrode potential amplitude) we can multiply the solution by  $\cos \omega t$  to introduce time dependence. In the sections that follow, we'll first introduce a toy model to better understand the effect of various parameters. We then present a more realistic model with data produced using COMSOL multiphysics.

According to Maxwell's equations, the EFG tensor is traceless and symmetric, and thus only has five independent components.

$$\dot{V} = \begin{pmatrix} V_{xx} & V_{xy} & V_{xz} \\ V_{xy} & V_{yy} & V_{yz} \\ V_{xz} & V_{yz} & -V_{xx} - V_{yy} \end{pmatrix}$$
(3.1)

In the general case, we consider a magnetic field at an angle  $\theta$  with respect to the z-axis. This is equivalent to the electrode apparatus being rotated around the x-axis by an angle  $\theta$ . This would yield an EFG

 $\underline{V} = R_x(\theta)\underline{V}_0R_x(\theta)^T$  where  $R_x(\theta)$  is the usual rotation matrix about the x-axis.

In practice  $V_{xy}$ ,  $V_{xz}$ ,  $V_{yz}$  will be negligible. Indeed, the antennae we will consider will have axes of symmetry along x, y and z, and we can expect the same axes to coincide with the principal axes of the tensor (in particular, it is a symmetric tensor, and therefore diagonalizable).

This yields Rabi angular frequencies  $\Omega_1$  and  $\Omega_2$  for transitions of one and two units of spin respectively:

$$\begin{cases}
\Omega_1 \approx \frac{\sqrt{3}eQ}{12\hbar} |V_{xx}\sin(2\theta)| \\
\Omega_2 \approx \frac{\sqrt{3}eQ}{24\hbar} |V_{xx}| (\cos(2\theta) + 3)
\end{cases}$$
(3.2)

The two frequencies cannot be equal. Nevertheless, for  $\theta \approx 58^{\circ}$ , we can minimize the square distance between the two and obtain a reasonable compromise. It might be useful to have distinct Rabi frequencies so as to be able to experimentally distinguish between the two transitions upon detection. Nevertheless, both frequencies ought to have a similar order of magnitude, to ensure they are both detectable. We therefore get the following angular frequencies:

$$\begin{cases} \Omega_1 \approx \frac{0.13eQ}{\hbar} |V_{xx}| \\ \Omega_2 \approx \frac{0.18eQ}{\hbar} |V_{xx}| \end{cases}$$
 (3.3)

According to (3.2), in order to achieve Rabi frequencies of 1 MHz, one needs to produce an EFG of the order of  $10^{21} \,\mathrm{V}\,\mathrm{m}^{-2}$ . Frequencies of the order of a megahertz are interesting, in that they allow over 10000 quantum gates to be applied within 10 ms, a coherence time reachable for nuclei. In practice, this EFG requires very high voltages on the electrodes, of the order of a megavolt, which in turn suggests a spacing between 10 nm and 100 nm through dimensional analysis as a first guess. These voltages are extremely hard to maintain. For comparison, the breakdown voltage of air for an electrode separation of the order of 100 nm is only around 0.3 V, while that of a perfect vacuum is 10<sup>11</sup> V. In practice, high vacuums can achieve breakdown voltages of the order of 10 to several 100 V. This is still very low compared to the target voltages, and it seems these can only be achieved under idealized conditions.

### 3.2 A toy model

Let's consider a sphere of surface potential  $V_0$  and radius R. Suppose the electric potential cancels at infinity. The unique solution to this problem (Laplace equation with Dirichlet boundary conditions) in spherical coordinates is:

$$V(r) = \frac{V_0 R}{r} \tag{3.4}$$

This gives the following EFG for four electrodes in a quadrupole configuration:

$$\tilde{V} = \begin{pmatrix}
\frac{6RV_0a^2}{(a^2+d^2)^{\frac{5}{2}}} & 0 & 0\\
0 & -\frac{6RV_0a^2}{(a^2+d^2)^{\frac{5}{2}}} & 0\\
0 & 0 & 0
\end{pmatrix}$$
(3.5)

we can then use (3.2) in conjunction with (3.5) to determine the Rabi frequency. In order to reach optimal transition times, the principal component of this EFG needs to be maximized. Clearly,  $V_{xx}$  decreases with d. However, for fixed d, there exists a value of a which maximizes the EFG and the Rabi frequency. We have:

$$\frac{\partial\Omega}{\partial a} = 0 \Longleftrightarrow a = \sqrt{\frac{2}{3}}d\tag{3.6}$$

Thus, the optimal solution in a gives a dependence in  $d^{-3}$  of the Rabi frequency.

### 3.3 A realistic model

### 3.3.1 Cubic electrodes

Although the previous model is a simplified version of the realistic electrodes, we can draw inspiration from it to propose a more general function which fits COMSOL predictions relatively well. In all the simulations, we use voltage amplitudes of 1 V, in order to predict Rabi frequencies per electrode voltage, since one can simply multiply the result by the desired amplitude to generalize to an arbitrary case.

We use the following ansatz for the EFG:

$$V_{xx} = c_1 \frac{(a - c_2)^2}{\left((a - c_2)^2 + (d - c_3)^2\right)^{\frac{5}{2}}}$$
(3.7)

where  $c_1$ ,  $c_2$  and  $c_3$  are fitting parameters. We then use the method of least squares to approximate the data generated using COMSOL.

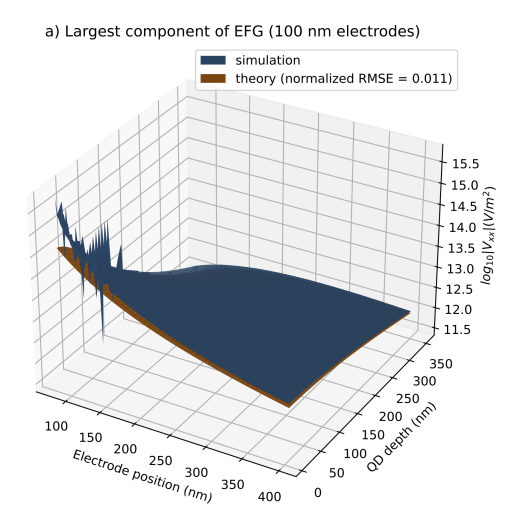
Thus, once we simulate the EFG, we can use the previous analysis and consider a time-dependent perturbation of the same form as (2.2). Since the nuclei in the QDs studied in this work are gallium and arsenic, and their quadrupole moments are of the same order of magnitude, one can focus on the naturally abundant gallium isotope without loss of generality. For this isotope,  $Q = 165 \,\text{mb} = 1.65 \cdot 10^{-29} \,\text{m}^2$  [34].

We first consider the closest situation to that of the toy model achievable using electron-beam lithography. Indeed, the electrodes are made using gold deposited on the semiconductor substrate, and as such the geometry has to be invariant along the growth axis. Thus, one can start by considering cubic electrodes of side 100 nm and 10 nm for example, to gauge how the relevant quantities scale with electrode size.

Figure 3 shows that the COMSOL results can be approximated very well by a function that varies like in the spherical case. The fit is better for smaller electrodes, since it approaches a point-like scenario, which is equivalent to a sphere according to Gauss's theorem. Furthermore, the geometric parameters yielding optimal EFGs in figure 4 fit the ideal theory remarkably well, and the divergences at lower depth can be explained by the fact that the optimal configuration for the electrodes can no longer be reached because the electrodes are too big in the 100 nm case. The same explanation can be given for differences observed in figure 5. Moreover, figure 6 shows that the previous estimate for the electrode separation was too optimistic, since even 10-100 nm separation fails to yield megahertz-range Rabi frequencies.

### 3.3.2 Elongated electrodes with pointed extremities

Here, we consider electrodes with a higher degree of anisotropy. The quadrupole electrodes considered here are elongated, cuboid-like with a pointed extremity, pointing towards the area where the addressed QDs are. The electrodes that are studied here have a height of 100 nm, a length of 200 nm, and a



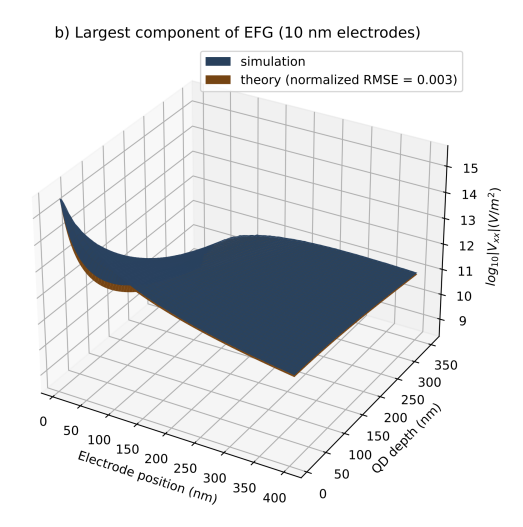


Figure 3: EFG as a function of antenna geometry. Electrode position refers to the distance between the origin and the center of a given electrode. The RMSE is dimensionless and normalized to the spread of the EFG values. a)  $c_1 = 2.38 \cdot 10^{-7}$ ,  $c_2 = 0$ ,  $c_3 = 0$ . b)  $c_1 = 2.29 \cdot 10^{-8}$ ,  $c_2 = 0$ ,  $c_3 = 0$  SI.

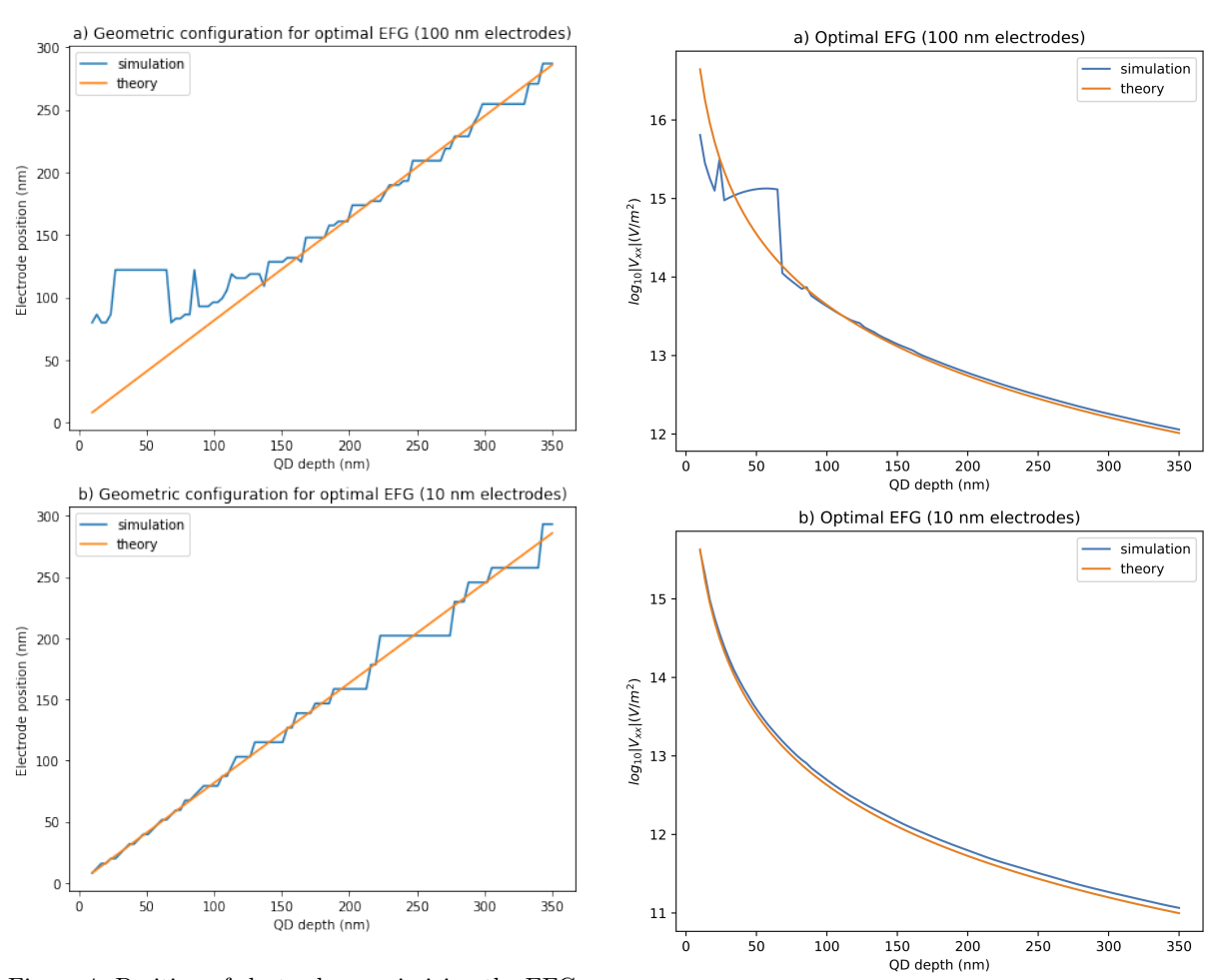
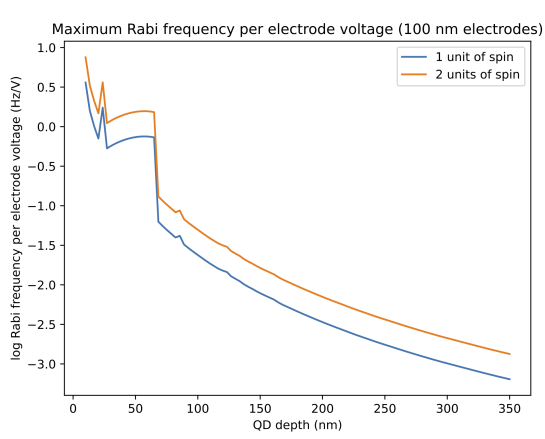


Figure 4: Position of electrodes maximizing the EFG for a given QD depth.

Figure 5: Maximum EFG for given QD depth.



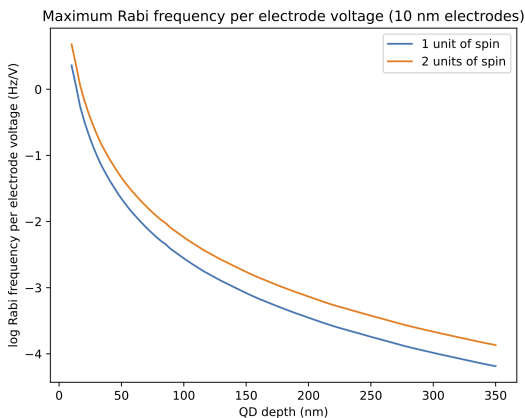


Figure 6: Rabi frequencies for nuclear spin transitions (of one or two units of spin) at a given QD depth for optimal EFGs and cubic electrodes of 10 nm or 100 nm

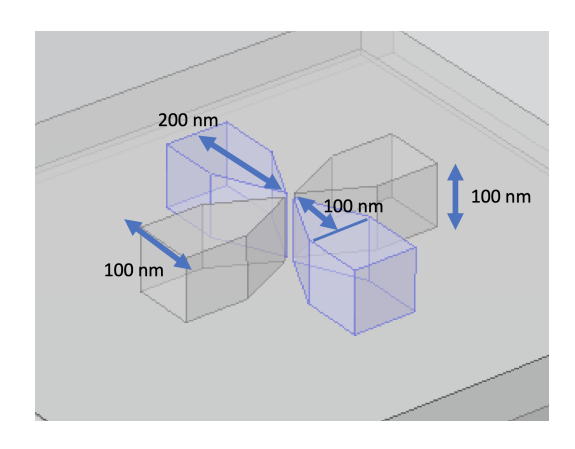


Figure 7: Quadrupole antenna with elongated electrodes (COMSOL).

pointed extremity of height 100 nm. In this section, the position of an electrode refers to the distance between the origin and a given electrode's pointed tip (figure 7).

Admittedly, this case is less symmetric than the previous one, but we can still try to fit a similar model. In fact, we can use the spherical toy model, and suppose that a given electrode can be approximated fairly well by a set of spheres arranged along a line. This case can be solved analytically, and yields the following EFG, p being the number of spheres representing an electrode:

$$V_{xx} = \frac{6pRV_0 (2(p-1)R + a)^2}{\left( (2(p-1)R + a)^2 + d^2 \right)^{\frac{5}{2}}}$$
(3.8)

The length of a given electrode in this model is L=2Rp. Thus, ignoring the constant factor, this function behaves as though the center of charge of the system were in the furthest sphere.

The maximum EFG is achieved for

$$a = \sqrt{\frac{2}{3}}d - 2(p-1)R = \sqrt{\frac{2}{3}}d - \frac{p-1}{p}L$$
 (3.9)

Thus, in order to observe a maximum, we approximately need  $L \lesssim d$ . We will use  $R = \frac{w}{2}$  where w

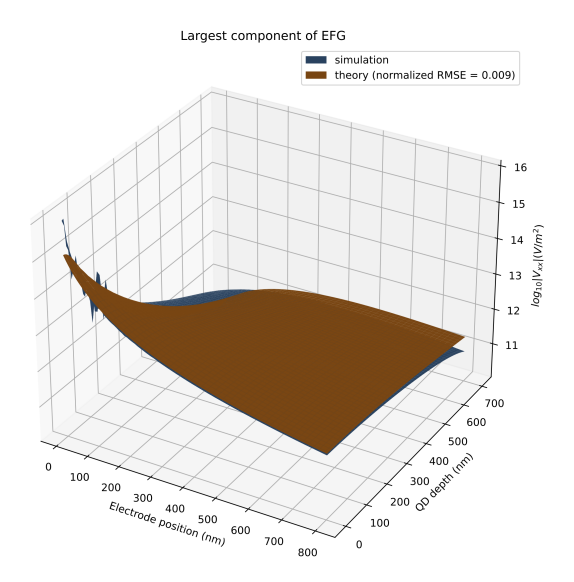


Figure 8: EFG as a function of antenna geometry. Electrode position refers to the distance between the origin and the tip of a given electrode. The RMSE is dimensionless and normalized to the spread of the EFG values.  $c_1 = 4.69 \cdot 10^{-9}, c_2 = -6.46 \cdot 10^{-8}, c_3 = -1.50 \cdot 10^{-9}$  SI.

is the width of the electrodes used in the model, and

 $p=\frac{L}{2R}.$  In this case as well, figures 8 and 9 suggest that this model adequately predicts EFGs. Furthermore, figure 9 confirms the offset predicted by (3.9) relative to the cubic case, and we observe divergences from the theoretical model for small depth, in accordance with the requirement  $L \lesssim d$ .

#### 4 Experimental considerations

### Resonant circuit driving of the antenna

In order to achieve the highest possible voltages for the quadrupole electrodes using lower generator voltages, experiments will need to make use of resonant circuits. To this end, we also need to know the capac-

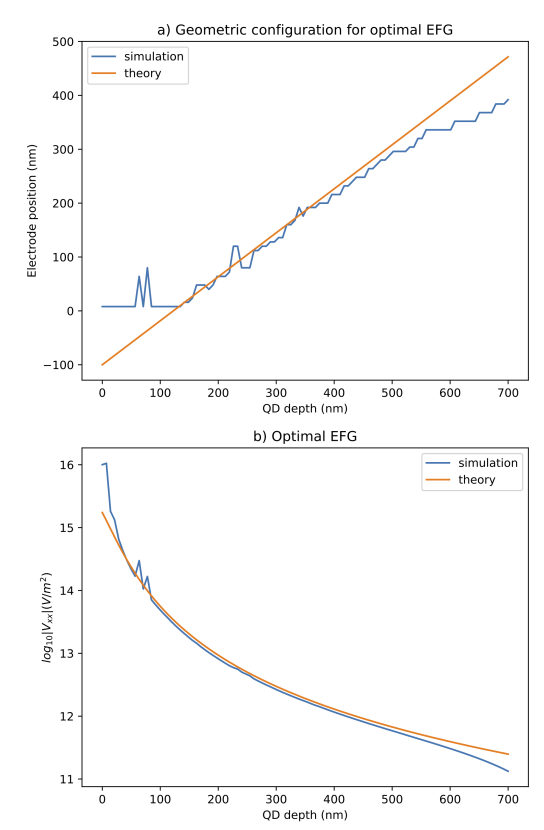


Figure 9: a) Position of electrodes maximizing the EFG for a given QD depth. The offset of the approximating affine function is correctly predicted using (3.9) for p=2 i.e. the number of spheres of width 100 nm one can fit on a line of 200 nm, the exact dimensions of the electrodes. b) Maximum EFG for given QD depth.

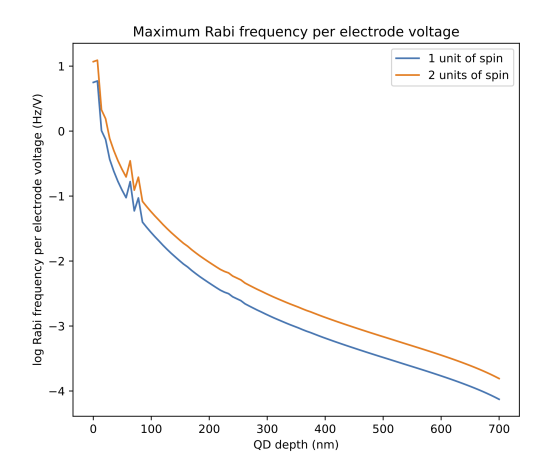


Figure 10: Rabi frequencies for nuclear spin transitions (of one or two units of spin) at a given QD depth for optimal EFGs and elongated electrodes.

itance between electrodes, and between an electrode and the ground plane. However, the net charge of the quadrupole antenna perceived by the ground plane is approximately zero, which means that the ground plane gets a negligible charge in practice. Hence, we will only focus on electrode-electrode capacitances.

Let us first return to our toy model to predict capacitance as a function of the position parameter a of the electrodes. Having computed the electric field generated by the apparatus, we can calculate the surface charges appearing on the electrodes, which are treated as ideal conductors. The interface conditions for electromagnetic fields yield:

$$\vec{E} - \vec{E}_{in} = \vec{E} = \frac{\sigma}{\varepsilon_r(\vec{n})\,\varepsilon_0}\vec{n} \tag{4.1}$$

Hence, the total charge appearing on an electrode is given by the following integral over its surface:

$$Q = \varepsilon_0 \oiint \varepsilon_r (\vec{n}) \vec{E} \cdot \vec{n} dS \qquad (4.2)$$

The capacitance between two given electrodes can be deduced from this by using  $C = \frac{Q}{2V_0}$  where  $V_0$  is the absolute value of the voltage boundary condition

on an electrode. We use the spherical toy model to approximate the cubic case as in the previous cases. We considering a single sphere at position  $\vec{r}$  and use spherical coordinates,  $\vec{n} = \vec{n} \, (\theta, \phi)$ . We suppose that a surface S of a given face of the cube/sphere is sufficiently small, such that:

$$Q \approx \varepsilon_r \varepsilon_0 \left( E_z \left( \vec{r} + \vec{e}_z \right) + E_z \left( \vec{r} - \vec{e}_z \right) \right)$$

$$+ \varepsilon_0 \sum_{r=0}^{3} \vec{E} \left( \vec{r} + \vec{e}_i \right) \cdot \vec{n} \left( \frac{\pi}{2}, \frac{n\pi}{2} \right)$$

$$(4.3)$$

This approximation yields a very long formula. Nevertheless, we can Taylor expand for  $R \to 0$ :

$$C = \frac{\varepsilon_0 \left(\varepsilon_r + 5\right) S}{2R} + \frac{\varepsilon_0 SR}{4a^2} - \frac{\sqrt{2}\varepsilon_0 \left(\varepsilon_r - 1\right) SR^2}{4a^3} + \frac{\varepsilon_0 \left(3 + \varepsilon_r\right) SR^2}{16a^3} + \frac{3\varepsilon_0 SR^3}{16a^4} + S\mathcal{O}\left(R^4\right)$$
(4.4)

Using  $S = 4R^2$ :

$$C = 2\varepsilon_0 \left(\varepsilon_r + 5\right) R + \frac{\varepsilon_0 R^3}{a^2} - \frac{\sqrt{2}\varepsilon_0 \left(\varepsilon_r - 1\right) R^4}{a^3} + \frac{\varepsilon_0 \left(3 + \varepsilon_r\right) R^4}{4a^3} + \frac{3\varepsilon_0 R^5}{4a^4} + \mathcal{O}\left(R^6\right)$$

$$(4.5)$$

Using COMSOL to numerically calculate (4.2), we get the plots in figures 11 and 12. We also consider (4.5) as a function of a and determine the constants which best fit the data numerically. The models used in figure 4 are of the form:

$$C = k_1 + \frac{k_2}{a^2} + \frac{k_3}{a^3} + \frac{k_4}{a^4} + \frac{k_5}{a^5}$$
 (4.6)

where  $k_1$ ,  $k_2$ ,  $k_3$ ,  $k_4$  and  $k_5$  are given in the captions of figures 11 and 12.

For an RLC series circuit where the output is the voltage measured at the capacitor (the electrodes), the gain is given by:

$$G(\omega) = \frac{1}{\sqrt{(1 - LC\omega^2)^2 + R^2 C^2 \omega^2}}$$
(4.7)

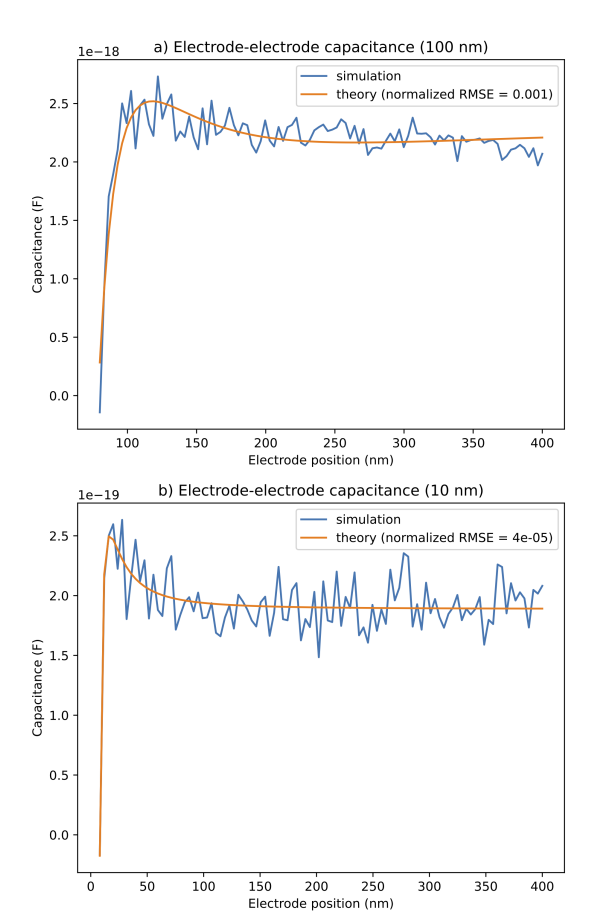


Figure 11: RMSE is dimensionless and normalized to average capacitance. a) Theory and simulation of capacitance between two oppositely charged cubic electrodes of side 100 nm, charge calculated using one electrode.  $k_1=2.4\cdot 10^{-18},\ k_2=-5.3\cdot 10^{-32},\ k_3=1.3\cdot 10^{-38},\ k_4=-8.3\cdot 10^{-46},\ k_5=0$  (SI units). b) Theory and simulation of capacitance between two oppositely charged cubic electrodes of side 10 nm, charge calculated using one electrode.  $k_1=1.9\cdot 10^{-19},\ k_2=5.9\cdot 10^{-35},\ k_3=-8.2\cdot 10^{-43},\ k_4=1.9\cdot 10^{-51},\ k_5=0$  (SI units).

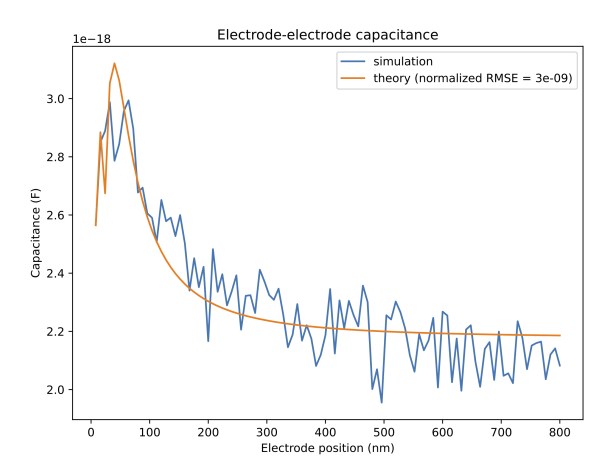


Figure 12: RMSE is dimensionless and normalized to average capacitance. Theory and simulation of capacitance between two oppositely charged elongated electrodes of length 200 nm, width 100 nm and pointed extremity of height 100 nm, charge calculated using one electrode.  $k_1 = 2.2 \cdot 10^{-18}$ ,  $k_2 = 6.4 \cdot 10^{-33}$ ,  $k_3 = -2.9 \cdot 10^{-40}$ ,  $k_4 = 4.1 \cdot 10^{-48}$ ,  $k_5 = -1.8 \cdot 10^{-56}$  (SI units).

where R and C are fixed by the transmission line and the capacitances modeled and simulated previously. Another parameter is the resonance frequency,  $\omega_0$ , which is fixed by the nuclear spin transitions considered i.e. the static magnetic field and the gyromagnetic ratio of the nuclei. For an RLC, we therefore have:

$$\omega_0^2 = \frac{1}{LC} - \frac{R^2}{2L^2} \tag{4.8}$$

Solving for the inductance gives:

$$L = \frac{1}{2C\omega_{res}^2} \pm \frac{1}{2C\omega_{res}^2} \sqrt{1 - 2R^2C^2\omega_{res}^2} \qquad (4.9)$$

The minus solution gives a small gain. We thus keep the plus solution. The capacitances plotted previously have a maximum. This can be determined analytically by canceling the derivative of the model. One ought to position the electrodes at the corresponding position, in order to minimize the inductance L necessary to drive the system at the resonant frequency. For a frequency of a megahertz, maximal capacitance for the 100 nm electrodes, B of the order of a tesla, this yields  $L\approx 100$  H. Plugging the inductance formula into (4.7), and taking into account the fact that  $RC\omega_0$  is small, we arrive at:

$$G = \frac{1}{RC\omega_0} \tag{4.10}$$

This is of the order of 10<sup>8</sup> in the scenario described above. In theory, we could reach the megavolt range and thus megahertz Rabi frequencies for a generator giving off a signal with an amplitude of 10 mV.

### 4.2 Canceling dipole fields

From an electromagnetism standpoint, AlGaAs is a nonlinear material, and as such the polarizability vector does not depend linearly on the electric field. This means that nonzero dipole fields can appear at the QD level, despite the electrode electric field being zero (see figure 13). These dipole fields will need to be canceled. Indeed, they can cause Stark shift of the electron energy levels, which we need to keep fixed.

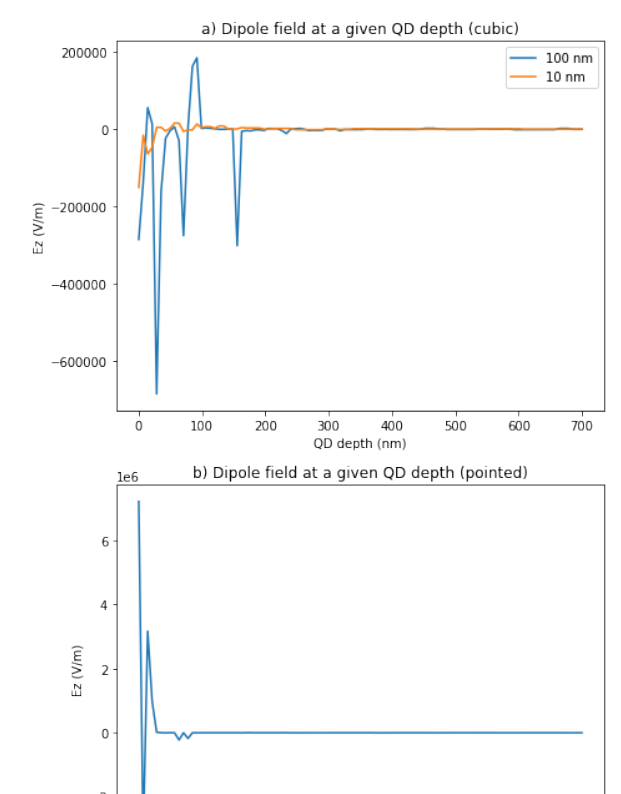


Figure 13: Dipole fields appearing along the z-axis due to the polarizability of AlGaAs: a) for cubic electrodes b) for elongated pointed electrodes.

300 400 QD depth (nm) 700

100

This can be remedied using a thin layer of gold covering the bottom of the semiconductor chip, such that the top surface is at a certain potential, and the lower one is the ground. If we want to cancel a field  $E_z$  at the QD level, one can use a potential  $V_0 = E_z(z_0 - z_1)$ where  $z_0$  is the position of the ground and  $z_1$  the position of the plane at nonzero potential. According to COMSOL simulations, the dipole fields are bounded by  $E_z = 1 \text{ MV/m}$ . If we take  $z_0 - z_1 = 10 \text{ nm}$ , the necessary voltage is  $V_0 = 0.01$  V. In practice, dipole fields need to be limited to 1 mV/500 nm, which approximately corresponds to shifting the exciton by one optical linewidth. This means that we can opt for an even smaller voltage. Furthermore, if the QDs are deep enough, at a depth of the order of 100 nm, which is usually the case in practice, then the dipole fields are of the order of 1 kV/m. Hence, at a sufficient depth, nothing needs to be done to counteract dipole fields.

### 5 Conclusion

Our findings show that NQR is theoretically feasible for driving nuclear spin transitions. We have shown that an AC quadrupole antenna etched onto an Al-GaAs sample can be used to drive QD nuclear transitions locally, and one could imagine an array of these quadrupoles on a semiconductor chip. The models and simulations presented here can aid experimentalists in the practical implementation of this system.

Previous sections have shown that the main challenges in NQR are related to obtaining sufficiently high Rabi frequencies and avoiding unwanted dipole fields in the material. Indeed, transition times need to be sufficiently low for efficient computation and coherence, while electric fields may shift the energy levels of the QD electron, which are meant to be kept fixed. The latter can be dealt with using a thin sheet of gold which produced an approximately constant electric field counteracting fields which appear at the QD level, while more work needs to be undertaken to address the former. We've addressed resonant circuit driving briefly, but this still requires very high voltages on the electrodes relative to the relevant breakdown voltages, regardless of the generator being sub-

ject to lower amplitudes thanks to the gain.

As mentioned previously, one could also implement NQR using strain waves which generate time-dependent EFGs. This will be addressed in future work.

# 6 Appendix: Derivation of the quadrupole Hamiltonian

In this section, we derive the classical potential energy of an electric quadrupole in an electric field. We first derive the quadrupole moment tensor.

Consider a charge distribution  $\{(q_i, \vec{OP_i})\}$ . We measure the field produced by the charges at a point M such that for all i,  $OP_i \ll OM$  where O is a point in the domain of the charge distribution. This yields the following expansion of the electric potential (V is no longer used for the EFG here):

$$V = \frac{1}{4\pi\epsilon_0} \sum_{i} \frac{q_i}{P_i M} = \frac{1}{4\pi\epsilon_0} \sum_{i} \frac{q_i}{\|P_i \vec{O} + O\vec{M}\|}$$

$$\approx \frac{Q}{4\pi\epsilon_0 OM} + \frac{\vec{p} \cdot O\vec{M}}{4\pi\epsilon_0 OM^3} + \frac{O\vec{M} \cdot Q \cdot O\vec{M}}{8\pi\epsilon_0 OM^5}$$
(6.1)

We've derived the monopole, dipole and quadrupole terms respectively, using the following tensors:

$$\begin{cases}
Q = \sum_{i} q_{i} \\
\vec{p} = \sum_{i} q_{i} \vec{OP}_{i} \\
Q = \sum_{i} q_{i} \left( 3\vec{OP}_{i} \otimes \vec{OP}_{i} - \vec{OP}_{i}^{2} \vec{I} \right)
\end{cases}$$
(6.2)

where I is the rank 2 identity tensor. Let's now turn our attention to the potential energy of a quadrupole in an electric field  $E_p$ . Here O is the origin of the coordinate system, and S is a point in the charge distribution domain. Let's consider the distance between the quadrupole and the source to be much greater than the dimensions of the quadrupole.

$$E_p = \sum_i q_i V(\vec{OP_i}) = \sum_i q_i V(\vec{OS} + \vec{SP_i})$$

$$\approx \sum_i q_i \left( V(\vec{OS}) + \nabla V \cdot \vec{SP_i} + \frac{1}{2} \vec{SP_i} \cdot \nabla^2 V \cdot \vec{SP_i} \right)$$

$$= QV - \vec{p} \cdot \vec{E} + \frac{1}{2} \sum_i q_i \vec{SP_i} \cdot \nabla^2 V \cdot \vec{SP_i}$$
(6.3)

where we've introduced the total charge Q and the electric dipole moment  $\vec{\mu}$  as defined previously. The last ingredient is the following calculation (which uses the Einstein summation convention):

$$Q: \nabla^2 V = \sum_i q_i \left( 3x_i^j x_i^k [\nabla^2 V]_{jk} - \delta^{jk} [\nabla^2 V]_{jk} \right)$$
$$= \sum_i q_i \left( 3S \vec{P}_i \cdot \nabla^2 V \cdot S \vec{P}_i - \text{Tr} \, \nabla^2 V \right)$$

The term with the trace is zero because of the Maxwell-Gauss equation:

$$\sum_{i} q_{i} \vec{SP}_{i} \cdot \nabla^{2} V \cdot \vec{SP}_{i} = \frac{1}{3} \vec{Q} : \nabla^{2} V$$
 (6.5)

Thus, we finally have

$$E_p = QV - \vec{p} \cdot \vec{E} + \frac{1}{6}Q : \nabla^2 V \tag{6.6}$$

Hence the following quadrupolar contribution (using the V notation for the EFG):

$$E_{p,Q} = \frac{1}{6} \dot{Q} : \dot{V} \tag{6.7}$$

While the EFG is referred to as the gradient of the electric field, it is actually defined as the Hessian of the electric potential (hence the absence of a minus sign).

The last step to understanding the quadrupole Hamiltonian in (2.1) is the Wigner-Eckart theorem. We define the quadrupolar moment by  $eQ = \langle I, I | Q_{zz} | I, I \rangle$  [30]. Because the quadrupole tensor is an irreducible spherical tensor of rank 2, we

need only calculate its spherical components  $Q_q^{(2)}$  for  $-2 \le q \le 2$ . According to the transformation rules from cartesian to spherical components (not to be confused with the classical spherical coordinates), we then have:

$$\langle I, I | Q_0^{(2)} | I, I \rangle = \sqrt{\frac{3}{2}} \langle I, I | Q_{zz} | I, I \rangle = \sqrt{\frac{3}{2}} eQ$$
(6.8)

According to the Wigner-Eckart theorem [33],  $Q^{(2)} \propto T^{(2)}$  where  $T^{(2)}$  is the irreducible spherical tensor of rank 2 constructed using the spin vector operator (see Sakurai for how to construct spherical tensor operators using spherical vector operators), and  $Q^{(2)}$  is the quadrupole tensor represented as an irreducible spherical tensor operator. Naming  $\alpha$  the proportionality factor:

$$\begin{split} \sqrt{\frac{3}{2}}eQ &= \alpha \left< I, I \right| T_0^{(2)} \left| I, I \right> \\ &= \alpha \left< I, I \right| \left( \frac{1}{\sqrt{6}} \left( 2\hat{I}_0^2 + \hat{I}_{+1}\hat{I}_{-1} + \hat{I}_{-1}\hat{I}_{+1} \right) \right) \left| I, I \right> \\ &= \frac{\alpha}{\sqrt{6}} \left< I, I \right| \left( 2\hat{I}_z^2 - \frac{1}{2}\hat{I}_+\hat{I}_- - \frac{1}{2}\hat{I}_-\hat{I}_+ \right) \left| I, I \right> \\ &= \frac{\alpha}{\sqrt{6}} I \left( 2I - 1 \right) \end{split}$$

$$(6.9)$$

Hence  $\alpha = \frac{3eQ}{I(2I-1)}$ . Incidentally, this proves that only nuclei of spin I > 1/2 can exhibit an electric quadrupole moment. This yields:

$$Q^{(2)} = \frac{3eQ}{I(2I-1)}T^{(2)} \tag{6.10}$$

We need to include the other components of  $T^{(2)}$  for the remaining calculations [30, 33]:

$$Q_0^{(2)} = \frac{3eQ}{\sqrt{6}I(2I-1)} \left(2\hat{I}_z^2 - \frac{1}{2}\hat{I}_+\hat{I}_- - \frac{1}{2}\hat{I}_-\hat{I}_+\right) \eqno(6.11)$$

$$Q_{\pm 1}^{(2)} = \mp \frac{3eQ}{2I(2I-1)} \left( \hat{I}_{\pm} \hat{I}_z + \hat{I}_z \hat{I}_{\pm} \right) \tag{6.12}$$

$$Q_{\pm 2}^{(2)} = \frac{3eQ}{2I(2I-1)} \left(\hat{I}_{\pm}\right)^2 \tag{6.13}$$

Next, we express the EFG tensor in spherical components. The EFG tensor is a rank-2 spherical tensor (traceless and symmetric via Maxwell's equations). Hence, its spherical components are given by the cartesian to spherical component transformations [33]:

$$V_0^{(2)} = \sqrt{\frac{3}{2}} V_{zz} \tag{6.14}$$

$$V_{\pm 1}^{(2)} = \mp V_{xz} - iV_{yz} \tag{6.15}$$

$$V_{\pm 2}^{(2)} = \frac{V_{xx} - V_{yy}}{2} \pm iV_{xy} \tag{6.16}$$

We finally get the result by contracting the spherical tensors according to their appropriate contraction rules (different from cartesian tensor rules):

$$\hat{H}_Q = \frac{1}{6} \sum_{q=-2}^{2} (-1)^q Q_q^{(2)} V_q^{(2)} = \frac{eQ}{2I(2I-1)} \hat{I} \cdot \hat{V} \cdot \hat{I}$$
(6.17)

### References

- 1. Deutsch, D. Quantum theory, the Church—Turing principle and the universal quantum computer. Proceedings of the Royal Society of London. A. Mathematical and Physical Sciences 400, 97–117 (1985).
- Nielsen, M. A. & Chuang, I. Quantum computation and quantum information 2002.
- 3. Grover, L. K. A fast quantum mechanical algorithm for database search in Proceedings of the twenty-eighth annual ACM symposium on Theory of computing (1996), 212–219.
- 4. Shor, P. W. Polynomial-time algorithms for prime factorization and discrete logarithms on a quantum computer. *SIAM review* **41**, 303–332 (1999).

- Feynman, R. P. in Feynman and computation 133–153 (CRC Press, 2018).
- Rabi, I. I., Zacharias, J. R., Millman, S. & Kusch, P. A New Method of Measuring Nuclear Magnetic Moment. *Phys. Rev.* 53, 318–318. https://link.aps.org/doi/10.1103/ PhysRev.53.318 (4 Feb. 1938).
- Levitt, M. H. Spin dynamics: basics of nuclear magnetic resonance (John Wiley & Sons, 2013).
- 8. Fox, A. M., Fox, M., et al. Quantum optics: an introduction (Oxford university press, 2006).
- 9. Clarke, J. & Wilhelm, F. K. Superconducting quantum bits. *Nature* **453**, 1031–1042 (2008).
- 10. Kok, P. et al. Linear optical quantum computing with photonic qubits. Reviews of modern physics **79**, 135 (2007).
- 11. Häffner, H., Roos, C. F. & Blatt, R. Quantum computing with trapped ions. *Physics reports* **469**, 155–203 (2008).
- Atatüre, M., Englund, D., Vamivakas, N., Lee, S.-Y. & Wrachtrup, J. Material platforms for spin-based photonic quantum technologies. Nature Reviews Materials 3, 38–51 (2018).
- 13. Ladd, T. D. *et al.* Quantum computers. *nature* **464**, 45–53 (2010).
- 14. Wu, C.-J. et al. A hybrid quantum photonic interface for 71Yb solid-state qubits. arXiv preprint arXiv:2212.01994 (2022).
- 15. Imamoglu, A. Are quantum dots useful for quantum computation? *Physica E: Low-dimensional Systems and Nanostructures* **16**, 47–50 (2003).
- Benson, O., Santori, C., Pelton, M. & Yamamoto, Y. Regulated and Entangled Photons from a Single Quantum Dot. *Phys. Rev. Lett.* 84, 2513-2516. https://link.aps.org/doi/10.1103/PhysRevLett.84.2513 (11 Mar. 2000).
- 17. Akopian, N. et al. Entangled Photon Pairs from Semiconductor Quantum Dots. Phys. Rev. Lett. 96, 130501. https://link.aps.org/doi/10.1103/PhysRevLett.96.130501 (13 Apr. 2006).

- 18. Taylor, J., Marcus, C. & Lukin, M. Long-lived memory for mesoscopic quantum bits. *Physical review letters* **90**, 206803 (2003).
- Gangloff, D. et al. Quantum interface of an electron and a nuclear ensemble. Science 364, 62–66 (2019).
- Gywat, O., Krenner, H. J. & Berezovsky, J. Spins in optically active quantum dots: concepts and methods (John Wiley & Sons, 2009).
- Mariette, H. Formation of self-assembled quantum dots induced by the Stranski-Krastanow transition: a comparison of various semiconductor systems. Comptes Rendus Physique 6, 23–32 (2005).
- Watanabe, K., Koguchi, N. & Gotoh, Y. Fabrication of GaAs quantum dots by modified droplet epitaxy. *Japanese Journal of Applied Physics* 39, L79 (2000).
- Urbaszek, B. et al. Nuclear spin physics in quantum dots: An optical investigation. Reviews of Modern Physics 85, 79 (2013).
- Boehme, C. & McCamey, D. R. Nuclear-spin quantum memory poised to take the lead. Science 336, 1239–1240 (2012).
- Chekhovich, E. et al. Nuclear spin effects in semiconductor quantum dots. Nature materials 12, 494–504 (2013).
- Zaporski, L. et al. Ideal refocusing of an optically active spin qubit under strong hyperfine interactions. Nature Nanotechnology, 1–7 (2023).
- Chekhovich, E. A., da Silva, S. F. C. & Rastelli,
   A. Nuclear spin quantum register in an optically active semiconductor quantum dot. *Nature Nanotechnology* 15, 999–1004 (2020).
- DiVincenzo, D. P. The physical implementation of quantum computation. Fortschritte der Physik: Progress of Physics 48, 771–783 (2000).
- Schimpf, C. et al. Hyperfine-interaction limits polarization entanglement of photons from semiconductor quantum dots. arXiv preprint arXiv:2302.05983 (2023).

- 30. Abragam, A. The principles of nuclear magnetism 32 (Oxford university press, 1961).
- 31. Jackson, D. *Initialisation*, control and readout of a nuclear-magnon quantum register PhD thesis (University of Cambridge, 2022).
- Denning, E. V., Gangloff, D. A., Atatüre, M., Mørk, J. & Le Gall, C. Collective quantum memory activated by a driven central spin. *Physical review letters* 123, 140502 (2019).
- Sakurai, J. J. & Commins, E. D. Modern quantum mechanics, revised edition 1995.
- 34. Pernpointner, M. & Schwerdtfeger, P. Accurate nuclear quadrupole moments of the gallium isotopes 69Ga and 71Ga within the PC-NQM model. *Chemical Physics Letters* **295**, 347–353. ISSN: 0009-2614. https://www.sciencedirect.com/science/article/pii/S0009261498009609 (1998).